



# IJRASET

International Journal For Research in  
Applied Science and Engineering Technology



---

# INTERNATIONAL JOURNAL FOR RESEARCH

IN APPLIED SCIENCE & ENGINEERING TECHNOLOGY

---

**Volume:** 14    **Issue:** III    **Month of publication:** March 2026

**DOI:** <https://doi.org/10.22214/ijraset.2026.78100>

[www.ijraset.com](http://www.ijraset.com)

Call:  08813907089

E-mail ID: [ijraset@gmail.com](mailto:ijraset@gmail.com)

# Green Synthesis of $\text{Bi}_2\text{MoO}_6$ NPs using *Euphorbia* Leaf Extracts for Removal of Toxic Organic Pollutant, Antibacterial and Antioxidant Performance

Prashant P. Mungle<sup>1</sup>, Priyadarshani N. Deshmukh<sup>2</sup>, Pravin K. Gaidhane<sup>3</sup>

<sup>1,2</sup>Department of Chemistry, Shri shivaji Education Society Amravati's Science College, Congress Nagar, Nagpur

<sup>3</sup>Department of Applied Chemistry, Govindrao Wanjari College of Engineering and Technology, Salai Godhani, Nagpur

**Abstract:** The investigation of instantaneous removal of multiple organic pollutants from using nanomaterials flags an innovative opportunity that is permitted from subordinate pollution and economical. In the aquatic atmosphere, river water contains large amount of organic effluent releases from the textile industries, which can stimulus the process of adsorption hence, the removal of toxic organic pollutant from the water bodies becomes a true challenge. Owing to this, we try to synthesize of  $\text{Bi}_2\text{MoO}_6$  NPs using *Euphorbia* leaf extracts as green reducing and capping agents, leaf extracts play a dual role to reduce both bismuth and molybdenum into corresponding metal oxide. As synthesized material were characterized various spectroscopic and microscopic techniques for the structural and morphological authentication. X-ray diffraction (XRD) confirmed the orthorhombic phase with crystalline size 10-12 nm. Elemental composition and purity of the NPs (Bi, Mo, C, and O elements) were confirmed via energy-dispersive X-ray spectroscopy (EDS). UV-DRS exposes band gap about 2.44 eV, which exhibited excellent semiconducting property for the removal of toxic compound. Surface area and pore size were assessed by Brunauer–Emmett–Teller (BET) analysis, obtained surface area found to be 82.66  $\text{m}^2/\text{g}$  and pore size was 9.9 nm. Morphological studies and particle size distribution were examined by scanning electron microscopy (SEM) and transmission electron microscopy (TEM), TEM revealed nearly spherical NPs with average particle size 30-35 nm. However, the adsorption studies revealed that  $\text{Bi}_2\text{MoO}_6$  NPs exhibit an outstanding removal efficiency for different dyes found to be 60.3, 79.5 and 66.8  $\text{mg g}^{-1}$  for Erichrome black T (EBT), Malachite green (MG) and Eosin yellow (EY) respectively. However, the kinetic studies follows pseudo-second order kinetics, and the equilibrium data authenticate for Freundlich and Langmuir isotherm. Furthermore,  $\text{Bi}_2\text{MoO}_6$  NPs showed excellent activity against *E. coli*, *S. aureus* followed by *B. subtilis* and *K. pneumoniae*. DPPH scavenging activity, in methanolic solvent showed higher radical inhibition than ethanolic solvent.

**Keywords:**  $\text{Bi}_2\text{MoO}_6$  NPs; *Euphorbia*; UV-DRS; EBT; DPPH; *K. pneumoniae*.

## I. INTRODUCTION

Nowadays rapid and incessant development of the world inhabitants has expressively increased the heaviness on the scientific society to address an assortment of environmental tasks, with water contamination emerging as a critical concern [1-2]. Industrial waste from organic pollutant, pharmaceutical, agricultural, and textile sectors pointedly contributes to water pollution, releasing dangerous constituents into aquatic ecosystems. Major pollutants in this wastewater include heavy metals, dyes, biodegradable organics, pesticides, pharmaceutical residues, and antibiotics [3-4]. These contaminants not only affect human health but also disrupt ecological balance.

Conventional wastewater treatment methods, such as adsorption [5], coagulation/flocculation [6], electrochemical treatment [7] and chemical precipitation [8], photodegradation [9] were used to eliminate organic pollutant from wastewater. Considering the efficiency and cost, adsorption is one of the widely recognized practices in the laboratory and everyday application [10, 11]. In recent years, many innovative and high-efficient nanomaterials (NMs) such as graphene, carbon based metal oxides and bismuth molybdate have been established to decontaminate the wastewater polluted by toxic organic dyes [12-14]. However, those NMs are portable in the environment and difficult to separate and reclaim, which gives increase to great vulnerability to the environment [15-16]. Furthermore, nanoscale range adsorbents agonise from unadorned stress drop in column processes, which obstructs their real-world application.

Therefore, there is a need to invent ways of assembling novel hybrids with large size and high adsorption capacity. In this context, the development of multifunctional and highly efficient materials for environmental mitigation remains a significant challenge for the scientific community [17]. Over the past decade, a wide range of advanced materials have been developed for environmental applications, particularly for the removal of pollutants from water and wastewater. Among them, metal, metal oxides and their composites have shown promising results due to their large surface area, chemical stability, and tunable surface functionalities. Materials like  $\text{TiO}_2$ ,  $\text{ZnO}$ , bismuth-based metal oxides, activated carbon, graphene oxide have been extensively investigated for adsorption, photocatalysis, and membrane filtration processes [18-20]. In particular, bismuth molybdate ( $\text{Bi}_2\text{MoO}_6$ ), a member of the Aurivillius family, exhibits promising properties such as high surface activity, tunable band structure, and strong oxidative capability, making it a potential candidate for biological and adsorption-based applications [21].

Conventionally,  $\text{Bi}_2\text{MoO}_6$  NPs are synthesized using methods such as hydrothermal, solvothermal, sol-gel, and co-precipitation techniques. Although effective, these approaches often involve high energy consumption, toxic chemicals, complex reaction conditions, and environmentally hazardous by-products [22]. In recent years, Plant-mediated synthesis has emerged as a simple, cost-effective, and scalable green approach due to the rich diversity of phytochemicals such as polyphenols, flavonoids, terpenoids, alkaloids, and proteins present in plant extracts. These bioactive compounds play a crucial role in the reduction of metal ions and stabilization of NPs, often imparting additional functional properties [23].

*Euphorbia*, commonly known as wild poinsettia, belongs to the family *Euphorbiaceae* and is widely distributed in tropical and subtropical regions. The plant is known for its rich phytochemical profile, including flavonoids, phenolic compounds, terpenoids, tannins, and glycosides. Traditionally, *Euphorbia* has been used in folk medicine for its antimicrobial, anti-inflammatory, antioxidant, and wound-healing properties [24]. These bioactive constituents make the plant an excellent candidate for use as a natural reducing and capping agent in the green synthesis of metal oxide NPs. In the present investigation, we report a green approach for the synthesis of  $\text{Bi}_2\text{MoO}_6$  NPs using *Euphorbia* leaves extract as a natural reducing agent. The extract assists the instantaneous reduction of Bi and the Mo precursor, leading to the formation of  $\text{Bi}_2\text{MoO}_6$  NPs. The green synthesized NPs were employed for the removal of toxic organic pollutants from aqueous media, and obtained result revealed that  $\text{Bi}_2\text{MoO}_6$  NPs show the maximum removal efficiency found to be 60.3, 79.5 and 66.8  $\text{mg g}^{-1}$  for EBT, MG and EY dyes respectively. However, the kinetic studies indicated that the adsorption process follows pseudo-second order kinetics, while the equilibrium data were well fitted with both *Freundlich* and *Langmuir* isotherm models. Furthermore,  $\text{Bi}_2\text{MoO}_6$  NPs showed excellent activity at a concentration of 0.1 $\text{mg}/100\mu\text{L}$  against gram-negative bacteria *E. coli* and gram-positive bacteria *S. aureus* followed by *K. pneumoniae* and *B. subtilis*. DPPH scavenging activity, in methanolic solvent showed higher radical inhibition than ethanolic solvent at higher concentration for the both  $\text{Bi}_2\text{MoO}_6$  NPs and leaf extracts.

## II. MATERIALS AND METHODS

### A. Materials

Bismuth nitrate pentahydrate [ $\text{Bi}(\text{NO}_3)_3 \cdot 5\text{H}_2\text{O}$ ,  $\geq 99\%$  purity] and sodium molybdate dihydrate [ $\text{Na}_2\text{MoO}_4 \cdot 2\text{H}_2\text{O}$ ,  $\geq 99\%$  purity] were procured from a commercial supplier and used as received. Fresh *Euphorbia* leaves were collected locally and authenticated prior to use. Sodium hydroxide (NaOH), methanol, 2,2-diphenyl-1-picrylhydrazyl (DPPH), and ascorbic acid were used for antioxidant studies. Methylene green, Eosine yellow, Erichrome black T dye was employed as a model adsorbate in adsorption experiments. Deionized water was used throughout the experiments. Nutrient agar, Mueller-Hinton agar, and standard antibiotics were procured from commercial suppliers and used without further purification.

### B. Characterization Techniques

The crystalline structure of the synthesized  $\text{Bi}_2\text{MoO}_6$  NPs was analyzed by X-ray diffraction (XRD) using  $\text{Cu K}\alpha$  radiation ( $\lambda = 1.5406 \text{ \AA}$ ) operated at 40 kV and 30 mA. Fourier transform infrared (FTIR) spectra were recorded in the range of 400–4000  $\text{cm}^{-1}$  to identify functional groups and phytochemical interactions. Surface morphology and particle size were examined using scanning electron microscopy (SEM) and transmission electron microscopy (TEM). Elemental composition was analyzed using energy-dispersive X-ray spectroscopy (EDX). Optical properties were evaluated using UV-diffuse reflectance spectroscopy (UV-DRS). The specific surface area was determined by Brunauer-Emmett-Teller (BET) analysis.

### C. Preparation of *Euphorbia* Plant Extract

Fresh *Euphorbia* leaves were washed thoroughly with tap water followed by deionized water and air-dried at room temperature. The dried leaves were finely chopped, and 10 g of plant material was added to 100 mL of deionized water. The mixture was heated at 80

°C for 30 min under continuous stirring. After cooling to room temperature, the extract was filtered using Whatman No. 42 filter paper. The obtained filtrate was stored at 4 °C and used within 48 h for nanoparticle synthesis.

#### D. Green synthesis of Bi<sub>2</sub>MoO<sub>6</sub> NPs

An aqueous solution of Bi(NO<sub>3</sub>)<sub>3</sub>·5H<sub>2</sub>O (0.05 M) was prepared by dissolving the precursor in 50 mL of deionized water under continuous stirring. Separately, a 0.05 M solution of Na<sub>2</sub>MoO<sub>4</sub>·2H<sub>2</sub>O was prepared in 50 mL of deionized water. To the bismuth nitrate solution, 20 mL of *Euphorbia* plant extract was added dropwise under constant stirring at 60 °C. Subsequently, the sodium molybdate solution was slowly introduced into the reaction mixture. The pH was adjusted to ~9 using 1 M NaOH solution. The mixture was stirred continuously for 4 h until the formation of a pale-yellow precipitate was observed. The precipitate was separated by centrifugation at 6000 rpm for 10 min, washed several times with deionized water and ethanol, and dried at 80 °C for 12 h. The dried powder was calcined at 450 °C for 3 h in a muffle furnace at a heating rate of 5 °C min<sup>-1</sup> to improve crystallinity and phase purity [25].

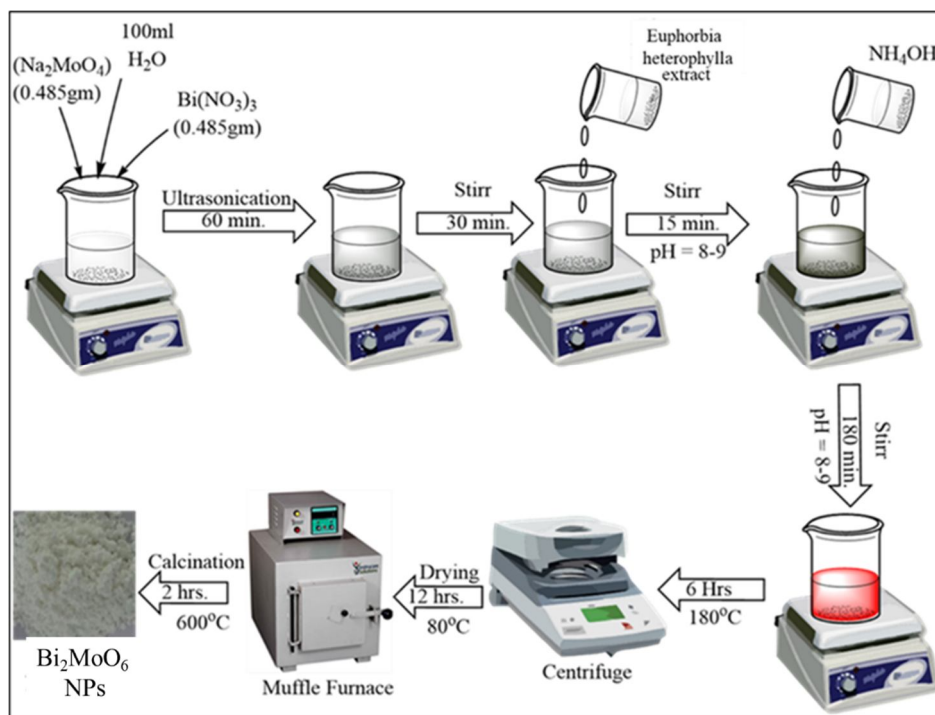


Figure 1: Scheme for the Synthesis of Bi<sub>2</sub>MoO<sub>6</sub> Nanoparticles

#### E. Adsorption Study of Dye

Batch adsorption experiments were conducted using various dye. A known amount of Bi<sub>2</sub>MoO<sub>6</sub> NPs (0.05 g) was added to 100 mL of EBT/MG/EY solution of dyes with initial concentrations ranging from 10 to 50 mg L<sup>-1</sup>. The mixture was stirred at 200 rpm at room temperature (≈25 °C). At specific time intervals, samples were withdrawn, centrifuged, and the residual dye concentration was measured at 500-700 nm using UV-visible spectroscopy [26].

The adsorption capacity ( $q_t$ ) and removal efficiency were calculated using:

$$q_t = \frac{(C_0 - C_t)V}{m}$$

$$\text{Removal efficiency (\%)} = \frac{(C_0 - C_t)}{C_0} \times 100$$

Where  $C_0$  and  $C_t$  are the initial and time-dependent dye concentrations (mg L<sup>-1</sup>),  $V$  is the solution volume (L), and  $m$  is the mass of adsorbent (g).

#### F. Adsorption Kinetics and Isotherm Models

##### Pseudo-First-Order (PFO) Model

$$\ln(q_e - q_t) = \ln q_e - k_1 t$$

Where  $q_e$  and  $q_t$  are the adsorption capacities ( $\text{mg g}^{-1}$ ) at equilibrium and time,  $t$ , respectively, and  $k_1$  ( $\text{min}^{-1}$ ) is the rate constant.

##### Pseudo-Second-Order (PSO) Model

$$\frac{t}{q_t} = \frac{1}{k_2 q_e^2} + \frac{t}{q_e}$$

Where  $k_2$  ( $\text{g mg}^{-1} \text{min}^{-1}$ ) is the PSO rate constant.

##### Langmuir Isotherm Model

$$\frac{C_e}{q_e} = \frac{1}{K_L q_{\max}} + \frac{C_e}{q_{\max}}$$

where  $C_e$  is the equilibrium concentration ( $\text{mg L}^{-1}$ ),  $q_{\max}$  is the maximum adsorption capacity ( $\text{mg g}^{-1}$ ), and  $K_L$  ( $\text{L mg}^{-1}$ ) is the Langmuir constant.

##### Freundlich Isotherm Model

$$\ln q_e = \ln K_F + \frac{1}{n} \ln C_e$$

Where  $K_F$  ( $(\text{mg g}^{-1}) (\text{L mg}^{-1})^{1/n}$ ) and  $n$  are *Freundlich* constants related to adsorption capacity and intensity.

#### G. Antibacterial Activity

The antibacterial activity of  $\text{Bi}_2\text{MoO}_6$  NPs was evaluated against several human pathogenic strains, including *S. aureus*, *E. coli*, *K. pneumonia* and *B. subtilis*. The antimicrobial efficacy was determined using the agar well plate method. *Mueller-Hinton* (MH) agar plates were equipped by standard protocols. Subsequently, 100  $\mu\text{L}$  of each bacterial culture was inoculated onto the agar surface and distributed uniformly using a sterile glass spreader. After the surface dried, wells with a diameter of 5 mm were bored into each culture dish using an agar borer to facilitate the loading of NPs (0.1mg/100  $\mu\text{L}$ ) samples followed by incubated at 37 °C. for 24 h, after incubation time completed, the zone of inhibition were observed/ measured using zone measuring scale reported in mm. Standard antibiotics were used as positive controls, while deionized water served as a negative control [27].

#### H. Antioxidant Activity

The antioxidant activity of the synthesized  $\text{Bi}_2\text{MoO}_6$  NPs was evaluated using the DPPH free radical scavenging assay. Nanoparticle suspensions with concentrations ranging from 25 to 200  $\mu\text{g mL}^{-1}$  were prepared in methanol [28]. A 2 mL aliquot of each suspension was mixed with 2 mL of 0.1 mM DPPH solution and incubated in the dark at room temperature for 30 min. The absorbance was measured at 517 nm using a UV-visible spectrophotometer. Ascorbic acid was used as a standard. The percentage radical scavenging activity was calculated as:

$$\text{Scavenging activity (\%)} = \left( \frac{A_0 - A_s}{A_0} \right) \times 100$$

Where  $A_0$  is the absorbance of the control and  $A_s$  is the absorbance of the sample.

### III. RESULTS AND DISCUSSION

#### A. XRD, FTIR, and EDS Analysis

The crystalline structure and phase purity of the green-synthesized  $\text{Bi}_2\text{MoO}_6$  NPs were investigated using XRD (fig.2). The diffraction pattern exhibits well-defined peaks at  $2\theta$  values corresponding to the *orthorhombic* phase of  $\text{Bi}_2\text{MoO}_6$ , in good agreement with standard (JCPDS No. 01-084-0787) data. The absence of impurity peaks confirms the successful formation of phase-pure  $\text{Bi}_2\text{MoO}_6$ .

The relatively broad diffraction peaks indicate the nanoscale nature of the particles. The average crystallite size  $\text{Bi}_2\text{MoO}_6$  NPs is 10–15 nm was calculated by the *Debye-Scherrer* equation.  $\text{Bi}_2\text{MoO}_6$  NPs confirming effective size control through the green synthesis route. The enhanced crystallinity observed after calcination at 450 °C further confirms the stabilization of the  $\text{Bi}_2\text{MoO}_6$  crystal structure [29].

Plane (hkl)	Approx. $2\theta$ (degree)
(020)	12°
(111)	23°
(131)	29°
(200)	33°
(151)	36°
(202)	46°
(133)	56°
(262)	60°

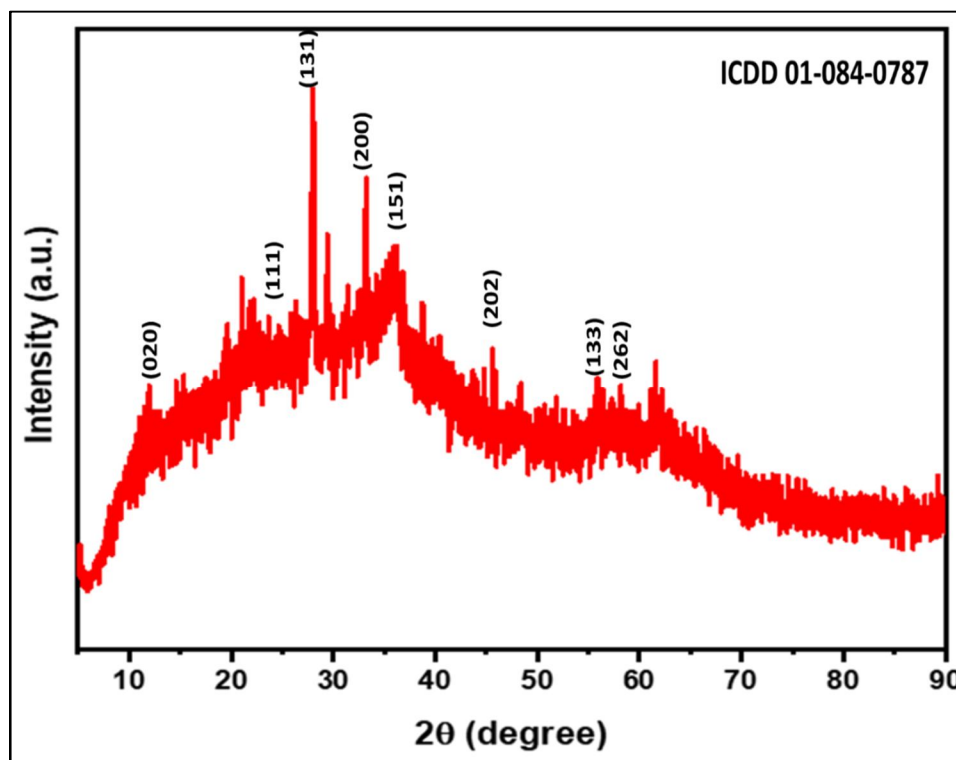


Figure 2: XRD of  $\text{Bi}_2\text{MoO}_6$  NPs

Fourier transform infrared (FTIR) spectroscopy was studied to identify the functional groups and phytochemical interactions intricate in the  $\text{Bi}_2\text{MoO}_6$  NPs. The FTIR spectrum shows absorption bands in the region of 400–800  $\text{cm}^{-1}$ , which are attributed to the stretching vibrations of Bi–O and Mo–O bonds, confirming the formation of the  $\text{Bi}_2\text{MoO}_6$  lattice. Broad bands observed around 3400  $\text{cm}^{-1}$  correspond to O–H stretching vibrations, indicating the presence of hydroxyl groups and adsorbed moisture of the sample (fig.2). Additional bands observed in the range of 1400–1650  $\text{cm}^{-1}$  are associated with C=O and C–O stretching vibrations, suggesting the involvement of plant-derived phytochemicals as capping and stabilizing agents on the surface of NPs [30].

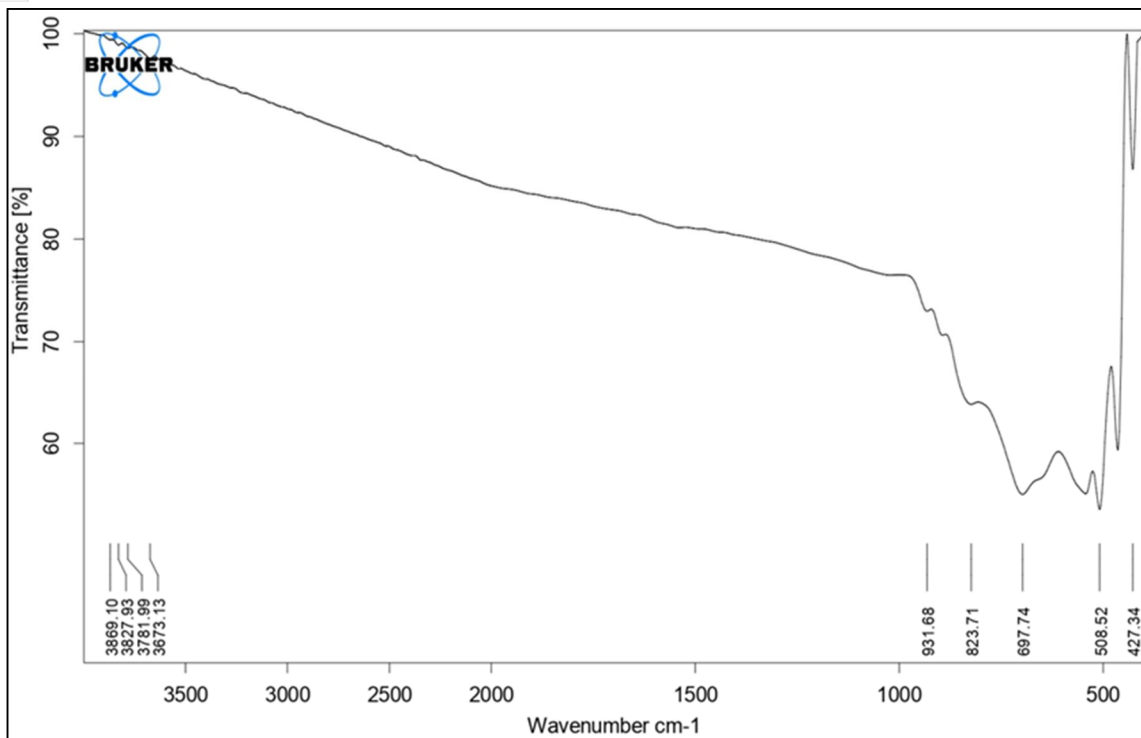


Figure 3: FTIR of  $\text{Bi}_2\text{MoO}_6$  NPs

Energy-dispersive X-ray spectroscopy (EDS) analysis was performed to confirm the elemental composition of the synthesized NPs. The EDS spectrum clearly reveals the presence of Bi, Mo, and O elements without any detectable impurities, confirming the high purity of the synthesized  $\text{Bi}_2\text{MoO}_6$  NPs [31]. The elemental ratios obtained from EDS analysis are in close agreement with the theoretical stoichiometry, further validating the successful synthesis via the green route. Also, an elemental analysis shows an existence of atomic percent {(Bi 48.20% and Mo 25.20% and O 26.70%)} for the synthesized materials in fig.4.

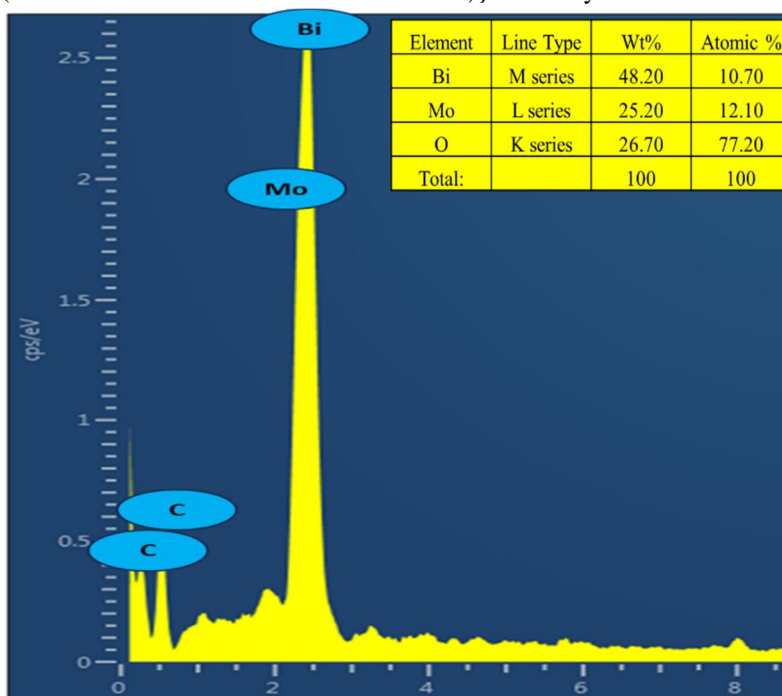


Figure 4: EDS of  $\text{Bi}_2\text{MoO}_6$  NPs

**B. UV-Diffuse Reflectance Spectroscopy (UV-DRS)**

The optical properties of the green-synthesized  $\text{Bi}_2\text{MoO}_6$  NPs were investigated using UV-diffuse reflectance spectroscopy (DRS). The DRS spectrum shows strong absorption in the visible light region, indicating the suitability of  $\text{Bi}_2\text{MoO}_6$  NPs for adsorption applications. The absorption edge was used to estimate the optical band gap energy by applying the *Kubelka–Munk* function shows in fig.5. Basically,  $\text{Bi}_2\text{MoO}_6$  NPs corresponds to *p*-type semi-conductor and absorption band gap ( $E_g$ ) can be determined by K-M plot using  $(\alpha h\nu)^2$  and  $h\nu$  values. The band gap energy from the K-M plot approximately 2.44 eV. The calculated band gap energy is found to be lower than that of bulk  $\text{Bi}_2\text{MoO}_6$ , which can be attributed to nanoscale size effects and surface modification by phytochemicals present in the *Euphorbia* extract [32].

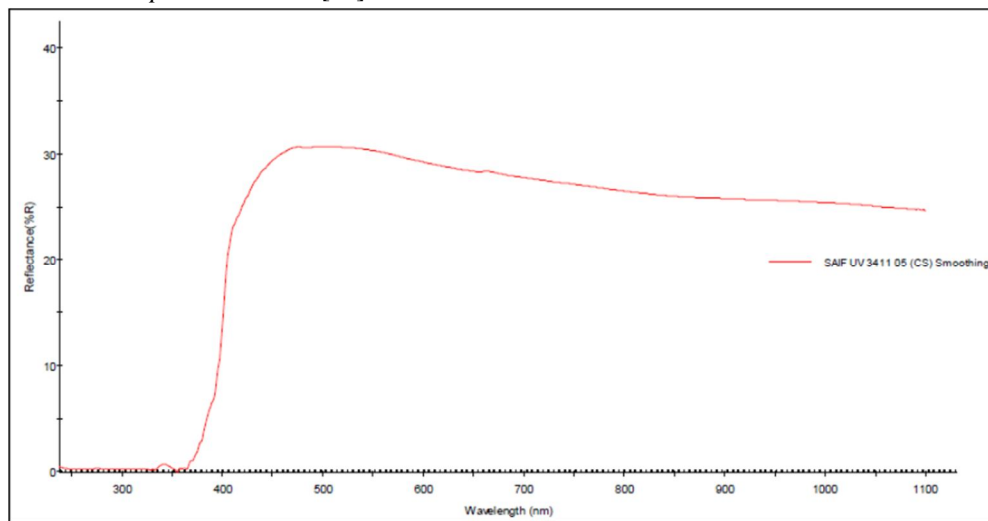


Figure 5: UV-DRS spectra of  $\text{Bi}_2\text{MoO}_6$  NPs

**C. BET Surface Area Analysis**

The textural properties of the synthesized  $\text{Bi}_2\text{MoO}_6$  NPs were evaluated using *Brunauer–Emmett–Teller* (BET) surface area analysis (fig. 6a). The nitrogen adsorption-desorption isotherm exhibits a type *IV* curve with a hysteresis loop, indicating the presence of mesoporous structures. The calculated specific surface area of the  $\text{Bi}_2\text{MoO}_6$  NPs found to be 82.66  $\text{m}^2/\text{g}$ , which is significantly high, which is valuable for surface-based applications. The pore size distribution, obtained using the *Barrett–Joyner–Halenda* (BJH) method (fig. 6b), confirms the presence of mesopores, the average pore size of the  $\text{Bi}_2\text{MoO}_6$  NPs is 9.9 nm which is enabling enhanced diffusion of dye molecules to the active sites. The large surface area and porous nature of the green-synthesized  $\text{Bi}_2\text{MoO}_6$  NPs contribute to their improved adsorption efficiency and antibacterial performance [33].

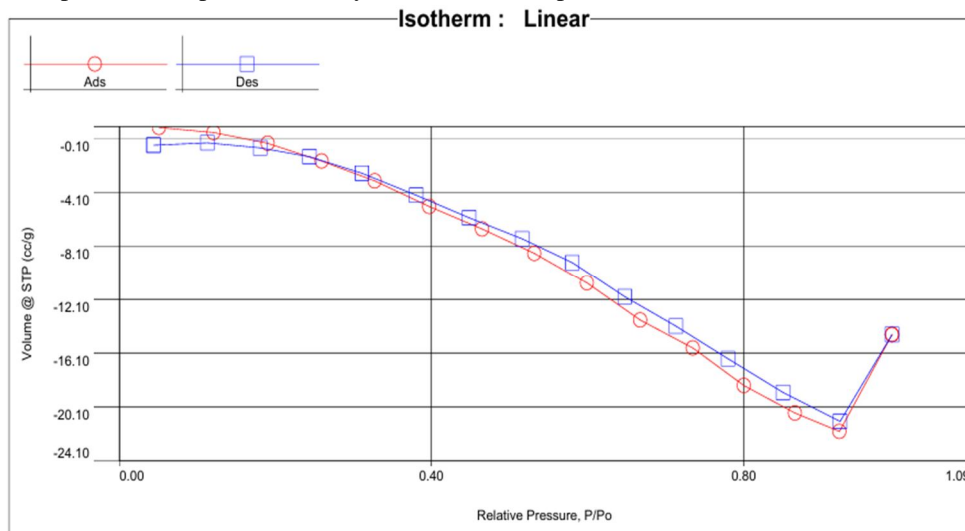


Figure 6a: BET of  $\text{Bi}_2\text{MoO}_6$  NPs

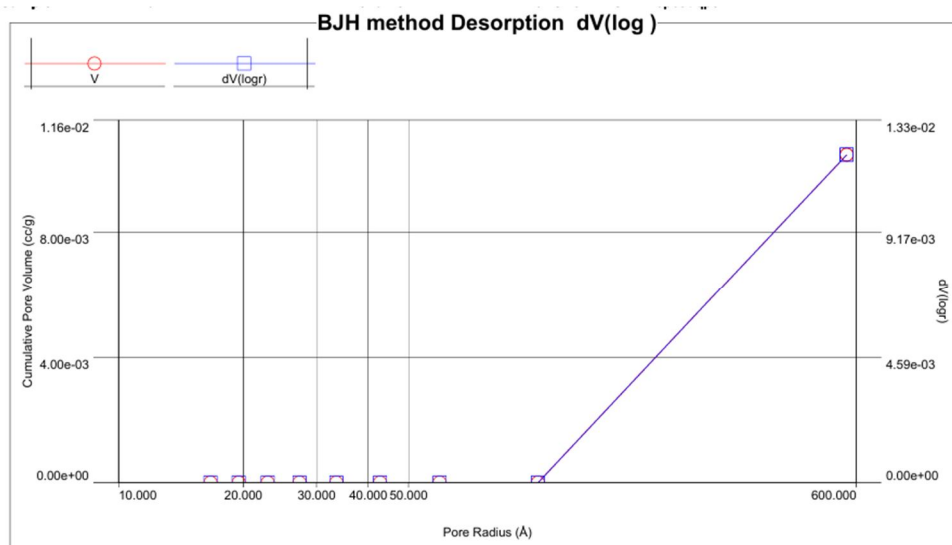


Figure 6b: Pore Size of Bi<sub>2</sub>MoO<sub>6</sub> NPs

#### D. Scanning Electron Microscopy (SEM)

The surface morphology of the synthesized Bi<sub>2</sub>MoO<sub>6</sub> NPs was examined using scanning electron microscopy (SEM). The SEM images reveal relatively uniform and well-distributed NPs with slight agglomeration, which is commonly observed in NMs due to high surface energy. The particles exhibit a quasi-spherical to irregular morphology, indicating effective nucleation and growth controlled by phytochemicals present in the *Euphorbia* extract in fig 7. The agglomeration observed in SEM images due to the interaction between surface molybdenum, bismuth metal oxides and capping agents of leaf extracts [34]. The average particles size of agglomerated NPs distributed uniformly across the surface having particle size nearly 180-220 nm.

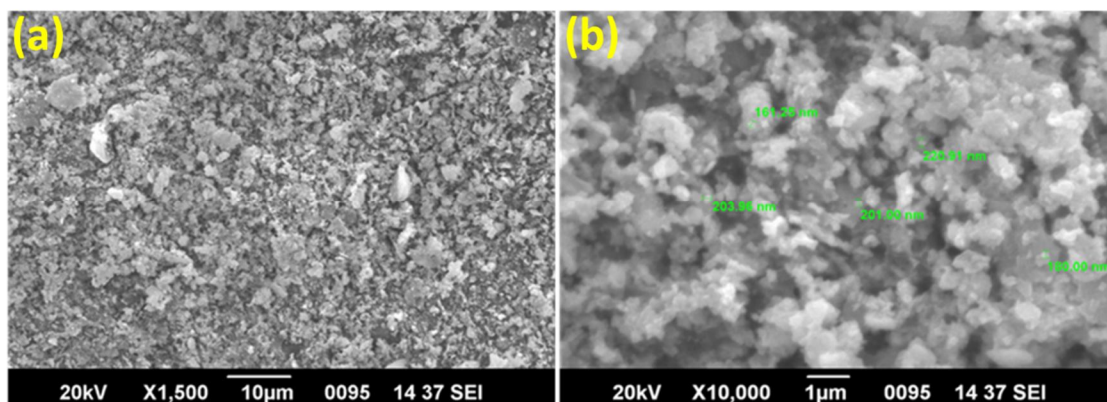
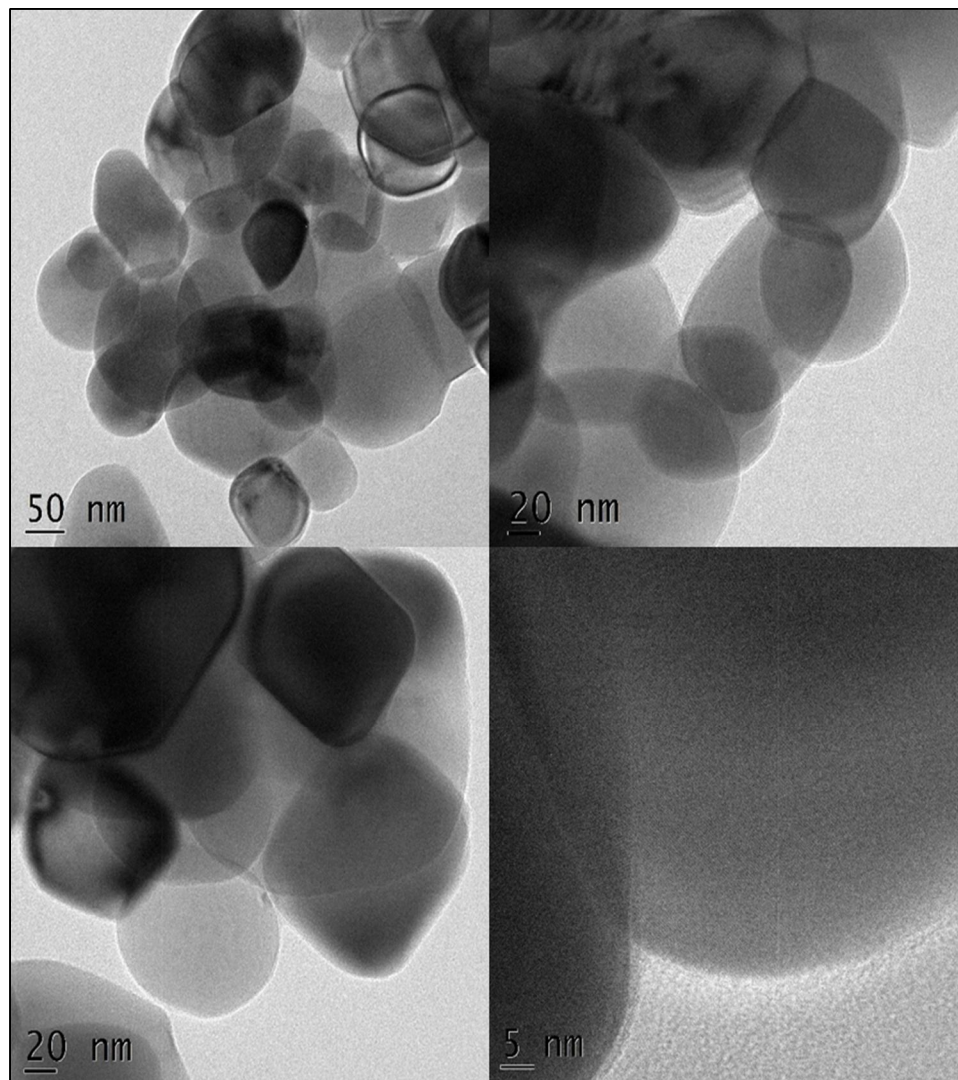


Figure 7: SEM images of Bi<sub>2</sub>MoO<sub>6</sub> NPs

#### E. Transmission Electron Microscopy (TEM)

Transmission electron microscopy (TEM) was employed to obtain detailed information on particle size, shape, and dispersion. The TEM images clearly show monodisperse Bi<sub>2</sub>MoO<sub>6</sub> NPs with an average particle size in the range of 30–35 nm. The particles exhibit well-defined margins and uniform contrast, authorising good crystallinity. Selected area electron diffraction (SAED) patterns display distinct concentric rings corresponding to the crystalline planes of Bi<sub>2</sub>MoO<sub>6</sub>, promote to confirming the polycrystalline nature of the NPs [35]. The narrow size distribution and good dispersion observed in TEM analysis highlight the effectiveness of the green synthesis approach in controlling nanoparticle growth and preventing excessive agglomeration and the formation spherical as well as globular NPs (fig. 8). The measured inter-planar spacing corresponds well with the (131) plane of *orthorhombic* Bi<sub>2</sub>MoO<sub>6</sub> NPs further validating the XRD results.

Figure 8: TEM images of  $\text{Bi}_2\text{MoO}_6$  NPs

#### IV. ADSORPTION STUDY

##### 1) Effect of Initial Metal Ion Concentration

The influence of initial metal ion concentration on the adsorption efficiency of  $\text{Bi}_2\text{MoO}_6$  NPs was investigated in the range of 10–60  $\text{mg L}^{-1}$ . The adsorption efficiency decreased gradually with increasing concentration for all dyes [36]. At lower concentrations, a higher percentage removal was observed due to the availability of abundant active sites on the adsorbent surface. However, as the concentration increased, the adsorption sites became saturated, resulting in a decrease in removal efficiency. Among the studied EBT (78%) exhibited the highest adsorption efficiency, followed by EY (76%) and MG (68%) indicating stronger binding affinity of  $\text{Bi}_2\text{MoO}_6$  NPs toward EBT dyes (Fig. 9a).

##### 2) Effect of Adsorbent Dose

The adsorption capacity increased significantly with increasing adsorbent dosage from 0.01 to 0.06 g. This enhancement can be attributed to the increased surface area and greater availability of adsorption sites. The removal efficiency reached maximum values at 0.05 g, beyond which the increase became marginal due to aggregation of NPs and overlapping of active sites. Thus, from the studies of adsorbent dose (0.05g) shows higher percentage of removal against all the dyes (fig. 9b). The removal efficacy for all the toxic dyes is higher ranges from 85-95%, the EBT shows higher removal capacity followed by EY and MG dyes.

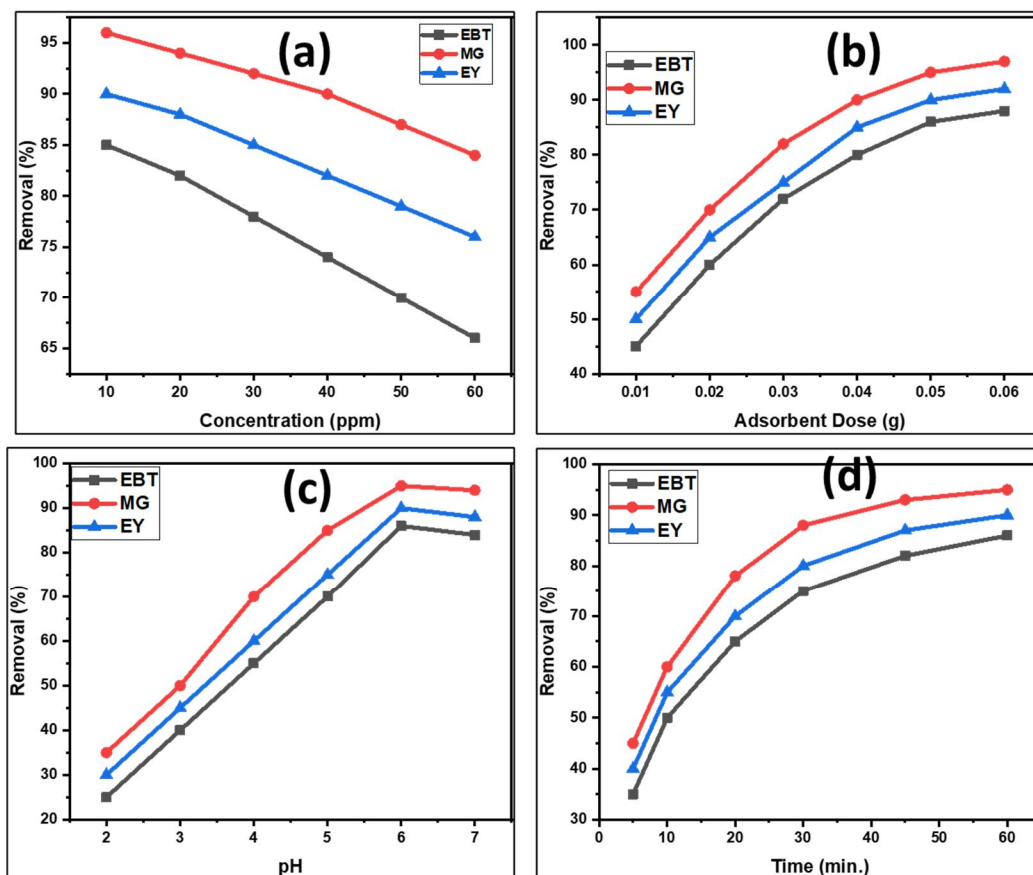


Figure 9: Effect of (a) Dyes concentration, (b) adsorbent doses, (c) pH, and (d) equilibrium time of toxic dyes (EBT, MG and EY) from an aqueous solution on  $\text{Bi}_2\text{MoO}_6$  NPs.

### 3) Effect of pH

The dyes solution having different pH plays a crucial role in the adsorption process as it affects both the surface charge of the adsorbent and the speciation of toxic dyes. The adsorption efficiency increased significantly from pH 2 to pH 6. At lower pH values, excessive  $\text{H}^+$  ions compete with organic moieties of dyes for the adsorption sites, resulting in lower adsorption. The optimum pH was observed around pH=6 where maximum adsorption occurred for all dyes (EBT MG and EY) using  $\text{Bi}_2\text{MoO}_6$  adsorbents. The removal efficiency for all the dyes ranges from 85-95% shows in fig. 9c.

### 4) Contact Time and Equilibrium Study

The adsorption process was rapid during the initial stage due to the availability of numerous active sites on the adsorbent surface in fig 9d. The adsorption rate gradually slowed as equilibrium approached. Equilibrium was achieved within 60 minutes for all the dyes (EBT MG and EY). The rapid adsorption performance specifies the strong interaction between the toxic dyes and  $\text{Bi}_2\text{MoO}_6$  NPs. The percentage of removal for all the toxic dyes is higher ranges from 82-92%.

### 5) Adsorption Isotherm Model

The equilibrium adsorption data were analyzed using *Langmuir* and *Freundlich* isotherm models in Table 1. The *Langmuir* model assumes monolayer adsorption on homogeneous surfaces, while the *Freundlich* model describes heterogeneous adsorption systems [37]. The calculated *Langmuir* maximum adsorption capacities ( $Q_{\text{max}}$ ) were found to be 60.3, 79.5 and 66.8  $\text{mg g}^{-1}$  for EBT, MG and EY dyes respectively. The high  $Q_{\text{max}}$  value for MG dyes confirms the strong adsorption capability of  $\text{Bi}_2\text{MoO}_6$  NPs compared with EBT and EY in fig 10a. However, the *Freundlich* maximum adsorption efficiency ( $K_f$ ) were observed 9.8 13.6 and 11.2  $\text{mg g}^{-1}$  for EBT, MG and EY dyes respectively. Thus from the *Langmuir* and *Freundlich* isotherm study exposed that the isotherms model well fitted in equilibrium data in fig 10b.

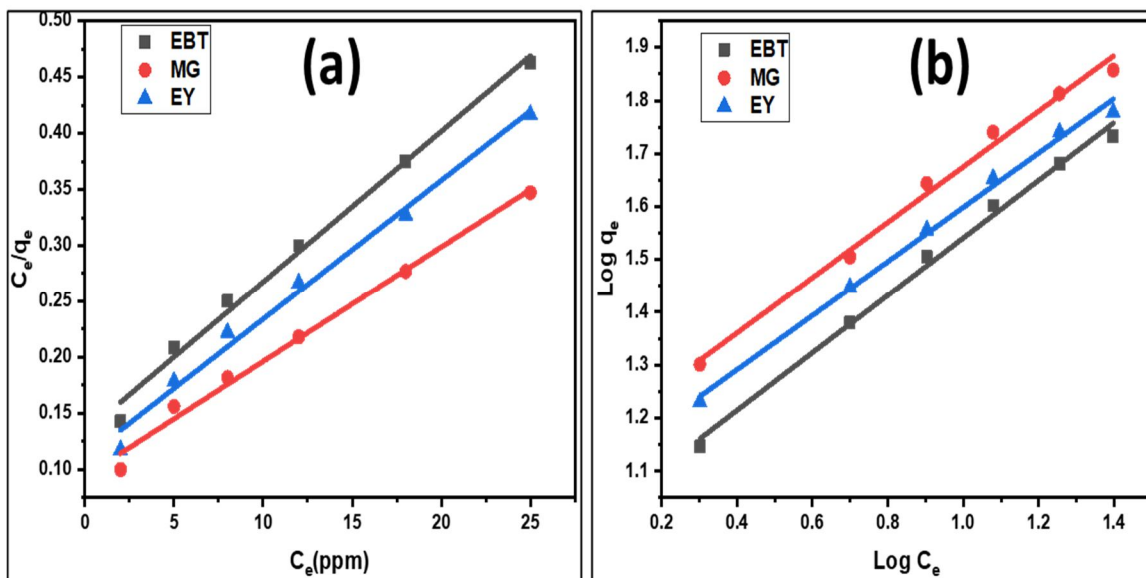


Figure 10: Isotherm models of  $\text{Bi}_2\text{MoO}_6$  NPs (a) *Langmuir* and (b) *Freundlich* for toxic dyes (EBT, MG and EY).

Table 1: *Langmuir* and *Freundlich* Isotherm Constants for Toxic Organic Dyes Adsorption onto  $\text{Bi}_2\text{MoO}_6$  NPs

Toxic Organic Dyes	Langmuir $Q_{\text{max}}$ ( $\text{mg g}^{-1}$ )	$KL$ ( $\text{L mg}^{-1}$ )	$R^2$ (Langmuir)	Freundlich $KF$	$n$	$R^2$ (Freundlich)
EBT	60.3	0.074	0.991	9.8	2.71	0.973
MG	79.5	0.092	0.995	13.6	3.05	0.980
EY	66.8	0.081	0.993	11.2	2.89	0.977

### 6) Adsorption Kinetics

The adsorption kinetics were evaluated using *pseudo-first-order* and *pseudo-second-order* models (fig 11a & b). The experimental data showed better agreement with the *pseudo-second-order* kinetic model, indicating that chemisorption involving valence forces or electron sharing between adsorbent and adsorbate is the rate-limiting step. From the adsorption kinetic study demonstrated that the coefficient relation value of pseudo order model found to be at unity for the *pseudo-second-order model*. Hence, kinetic data exposes well arrangement for the *pseudo-second-order* kinetic model [38].

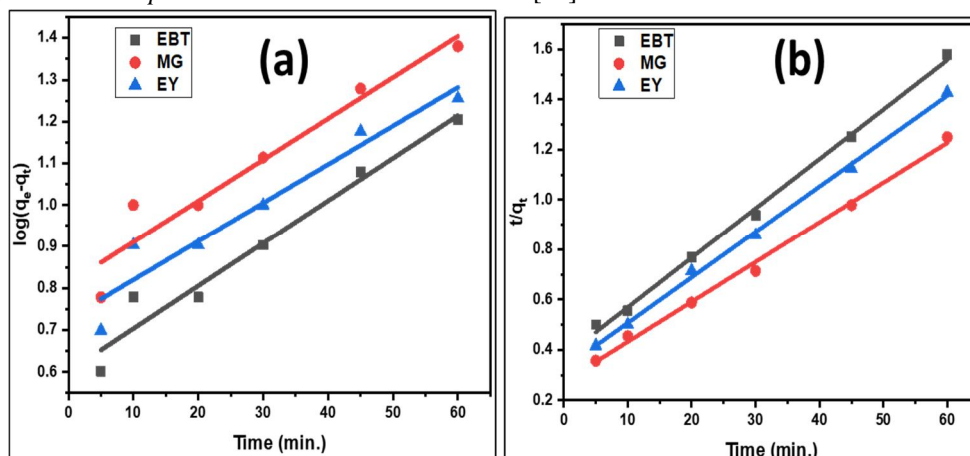


Figure 11: Kinetic models of  $\text{Bi}_2\text{MoO}_6$  NPs (a) *pseudo-first-order* and (b) *pseudo-second-order* models for toxic dyes (EBT, MG and EY).

Table 2: Kinetic Model Parameters for Toxic Organic Dyes Adsorption onto Bi<sub>2</sub>MoO<sub>6</sub> NPs

Toxic Organic Dyes	q <sub>e,exp</sub> (mg/g)	Pseudo-First-Order k <sub>1</sub> (min <sup>-1</sup> )	q <sub>e,cal</sub> (mg/g)	R <sup>2</sup> (PFO)	Pseudo-Second-Order k <sub>2</sub> (g mg <sup>-1</sup> min <sup>-1</sup> )	q <sub>e,cal</sub> (mg/g)	R <sup>2</sup> (PSO)
EBT	38	0.029	34.5	0.964	0.0021	39.2	0.998
MG	48	0.034	44.1	0.970	0.0026	49.5	0.999
EY	42	0.031	38.6	0.967	0.0023	43.0	0.998

A. Antibacterial Activity of Bi<sub>2</sub>MoO<sub>6</sub> NPs

In the present examination, the synthesized Bi<sub>2</sub>MoO<sub>6</sub> NPs employed for anti-bacterial studies as shown in [Fig. 12 (a-d)], this study was performed on human pathogenic bacteria. The antibacterial activity of NPs was initiated by UV light radiation. The antibacterial study of NPs was carried out at the concentration of 0.1mg/100µL against listed bacterial strain as *S. aureus*, *E. coli*, *K. pneumoniae*, and *B. subtilis*. The zone of inhibition obtained against selected bacterial strain as shown in [Fig. 12 (a-d)], suggests that strong inhibition zone was observed for gram-negative *E. coli* and gram-positive *S. aureus*. The significant result obtained for Bi<sub>2</sub>MoO<sub>6</sub> NPs with concentration of 0.1mg/100µL against gram-negative bacteria *E. coli* and gram-positive bacteria *S. aureus* followed by *K. pneumoniae* and *B. subtilis*. The comparative result obtained for anti-bacterial activity is listed (Table 3). The antibacterial assay was performed in triplicate [39].

Table 3: A comparative antibacterial activity of Bi<sub>2</sub>MoO<sub>6</sub> NPs

Pathogens	Standard Antibiotics n=3		Zone of inhibition* (mm) against pathogenic bacteria n=3
	(5µg/100µL) Ciprofloxacin	(5µg/100µL) Amikacin	
<i>S. aureus</i>	28±0.16	26±0.58	22±0.28
<i>E. coli</i>	29±0.16	23±0.54	23±0.16
<i>K. pneumoniae</i>	26±0.22	22±0.27	17±0.54
<i>B. subtilis</i>	21±0.28	24±0.36	13±0.36

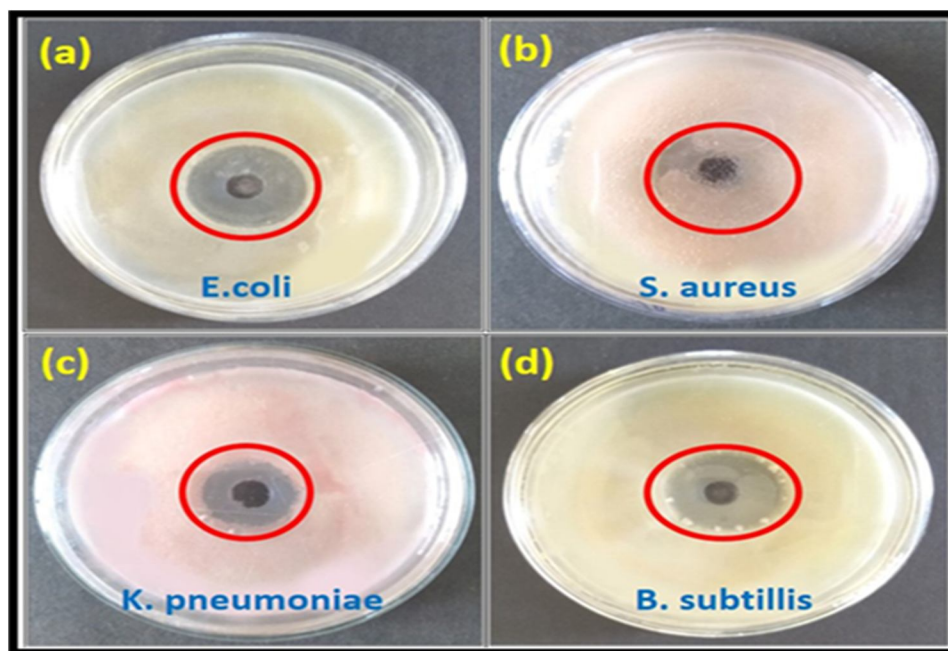


Figure 12: Zone of inhibition of pathogenic culture by Bi<sub>2</sub>MoO<sub>6</sub> NPs

**B. Antioxidant Activity of  $\text{Bi}_2\text{MoO}_6$  NPs**

The antioxidant property of *Euphorbia* mediated  $\text{Bi}_2\text{MoO}_6$  NPs was determined by using of DPPH ( $\alpha, \alpha$ -diphenyl- $\beta$ -picrylhydrazyl) method in Fig. 13.

Table 4: Antioxidant activity of *Euphorbia*,  $\text{Bi}_2\text{MoO}_6$  NPs by DPPH method

Treatment	Solvent	100 $\mu\text{g/mL}$	200 $\mu\text{g/mL}$	300 $\mu\text{g/mL}$	400 $\mu\text{g/mL}$	500 $\mu\text{g/mL}$
<i>Euphorbia</i> extract	Methanolic	62.68	71.89	74.66	78.37	85.62
$\text{Bi}_2\text{MoO}_6$ NPs	Methanolic	59.45	62.53	69.02	73.92	75.64
<i>Euphorbia</i> extract	Ethanolic	61.38	67.46	72.66	75.78	82.33
$\text{Bi}_2\text{MoO}_6$ NPs	Ethanolic	58.47	60.35	66.78	69.94	73.01
Standard	Ascorbic acid	75.17	78.20	80.33	82.16	89

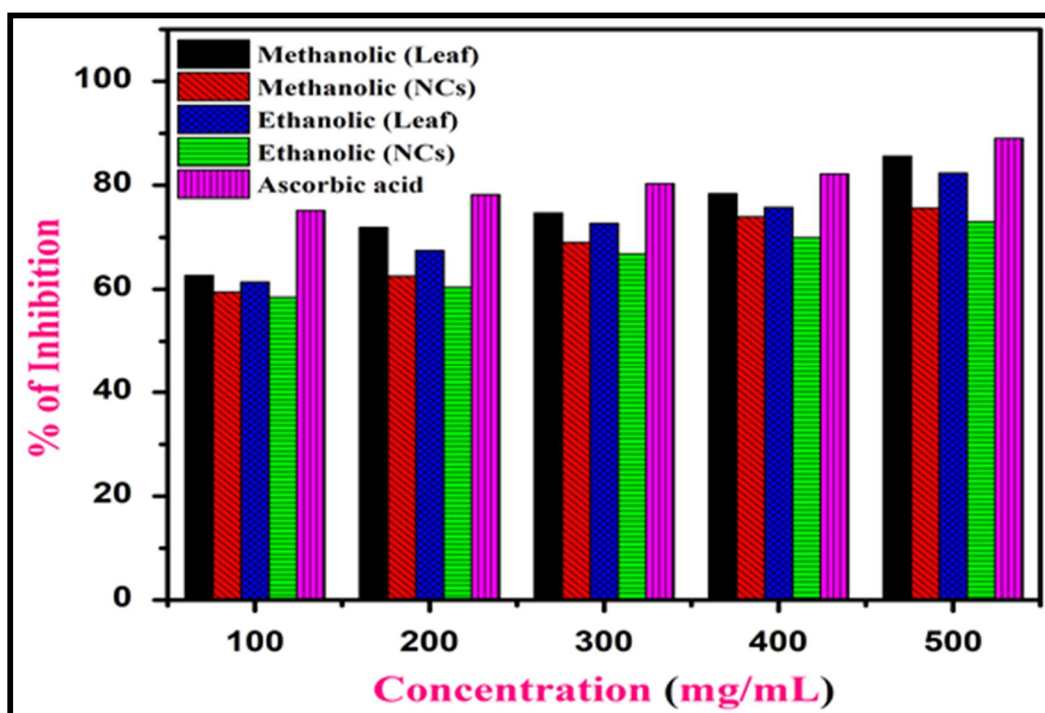


Figure 13: Antioxidant activity of *Euphorbia* leaf extracts,  $\text{Bi}_2\text{MoO}_6$  NPs by DPPH method

The results showed that among the used solvents, DPPH scavenging activity, in methanolic solvent showed higher radical inhibition activity than ethanolic solvent. The compared result with standard ascorbic acid in all concentration of assay, *Euphorbia* extract,  $\text{Bi}_2\text{MoO}_6$  NPs showed maximum inhibition at a concentration of 500  $\mu\text{g/mL}$  in both solvents. The possible reason corresponds to increased concentration of leaf extracts and NCs that increases scavenging activity of the materials [40]. Thus, owing to smaller particle grain size and may be a phenomenon of transfer of electron density from oxygen atom to odd electron located at nitrogen atom in DPPH, which results in decreasing transition intensity at 519 nm (Table 4).

**V. CONCLUSION**

In conclusion, the existing work fruitfully exposed the green synthesis of  $\text{Bi}_2\text{MoO}_6$  NPs using *Euphorbia* leaf extract, which performed a dual role as both the reducing and capping agent. As synthesized material were authenticate for their structural and morphological explorations techniques recognised the operative formation of the NPs. The TEM analysis exposed that of  $\text{Bi}_2\text{MoO}_6$  NPs having a size of nearly 30-35 nm. The result explored a single-phase orthorhombic phase. Furthermore, the NPs exhibited a large surface area of 82. 66  $\text{m}^2/\text{g}$ , confirming their mesoporous nature.

The Bi<sub>2</sub>MoO<sub>6</sub> adsorbent revealed a remarkable removal efficiency for MG, EY and EBT even at small doses, under environmentally conditions. The mechanistic methodology of adsorption kinetically scrutinized the *pseudo-second-order* kinetic model, while the equilibrium data were fitted for both *Langmuir* and *Freundlich* isotherms reinforced the surface interaction mechanisms between the NPs and organic toxic dyes. The maximum removal efficiency was found to be 60.3, 79.5 and 66.8 mg g<sup>-1</sup> for EBT, MG and EY dyes respectively. Moreover, Bi<sub>2</sub>MoO<sub>6</sub> NPs showed exceptional activity at a concentration of 0.1mg/100μL against *E. coli* (23 mm), *S. aureus* (22 mm) followed by *K. pneumonia* (17 mm) and *B. subtilis* (13 mm). The DPPH scavenging activity, in methanolic solvent showed higher radical inhibition activity than ethanolic solvent. The compared result with standard ascorbic acid in all concentration of assay, *Euphorbia* extract, Bi<sub>2</sub>MoO<sub>6</sub> NPs showed maximum inhibition at a concentration of 500 μg/mL in both solvents. In Complete, synthesized Bi<sub>2</sub>MoO<sub>6</sub> NPs offer an encouraging, workable solution for an effective elimination of toxic heavy metal ions from the aqua sphere as well as good sustainability against microbial pathogens.

## VI. ACKNOWLEDGMENTS

The authors are grateful to Head, Post Graduate Department of Chemistry and Microbiology, Shri Shivaji Education Society Amravati's Science College, Congress Nagar, Nagpur for proving laboratory facility to conduct adsorption study and antimicrobial activity.

Funding: None.

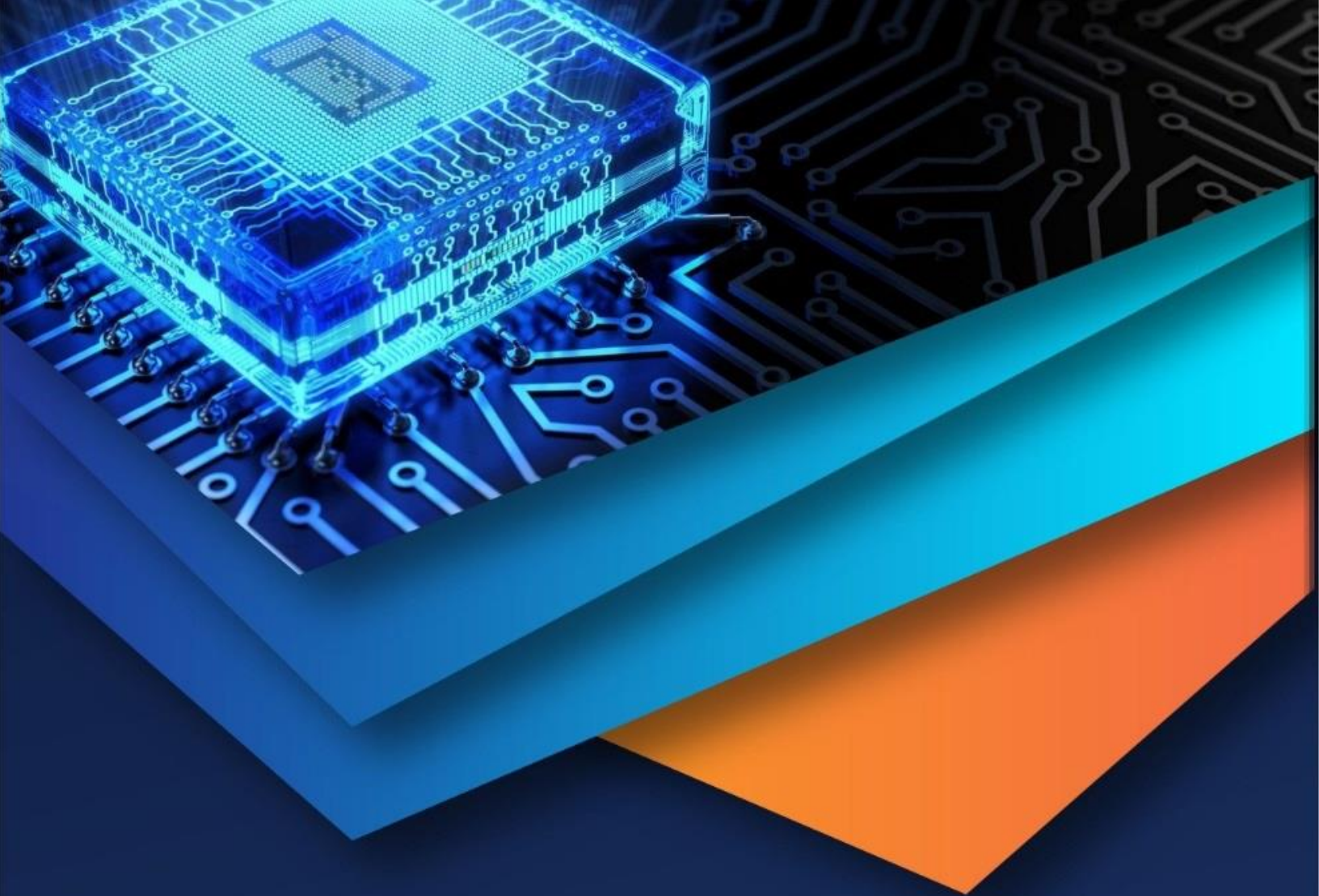
Conflict of Interest

The authors declare no conflict of interest, financial or otherwise.

## REFERENCES

- [1] K. Y. Kumar, H. B. Muralidhara, Y. A. Nayaka, J. Balasubramanyam, and H. Hanumanthappa, "Low-cost synthesis of metal oxide nanoparticles and their application in adsorption of commercial dye and heavy metal ion in aqueous solution," *Powder Technol.*, vol. 246, pp. 125–136, Sep. 2013, doi: 10.1016/j.powtec.2013.05.017.
- [2] R. Sarathi et al., "5 Journal of Chemical Reviews Photocatalytic Degradation of Malachite Green Dye by Metal Oxide Nanoparticles-Mini Review Photocatalytic Degradation of Malachite Green Dye by Metal Oxide Nanoparticles-Mini Review," *J. Chem. Rev.*, vol. 5, no. 1, 2023, doi: 10.22034/JCR.2023.
- [3] A. A. Sabrin A., "Textile Dye Removal from Wastewater Effluents Using Chitosan-ZnO Nanocomposite," *J Text Sci Eng.*, vol. 05, no. 03, 2015, doi: 10.4172/2165-8064.1000200.
- [4] D. Nayeri and S. A. Mousavi, "Dye removal from water and wastewater by nanosized metal oxides - modified activated carbon: a review on recent researches," *Journal of Environmental Health Science and Engineering*, vol. 18, no. 2. Springer Science and Business Media Deutschland GmbH, pp. 1671–1689, Dec. 01, 2020. doi: 10.1007/s40201-020-00566-w.
- [5] W. S. Al-Arjan, "Zinc Oxide Nanoparticles and Their Application in Adsorption of Toxic Dye from Aqueous Solution," *Polymers (Basel)*, vol. 14, no. 15, Aug. 2022, doi: 10.3390/polym14153086.
- [6] A. A. Alanazi, "Investigation of malachite green removal using graphene oxide-zinc oxide composite from aqueous solution: synthesis, characterization and application," *Desalination Water Treat.*, vol. 293, pp. 243–252, May 2023, doi: 10.5004/dwt.2023.29519.
- [7] S. Modi et al., "Recent and Emerging Trends in Remediation of Methylene Blue Dye from Wastewater by Using Zinc Oxide Nanoparticles," *Water (Switzerland)*, vol. 14, no. 11. MDPI, Jun. 01, 2022. doi: 10.3390/w14111749.
- [8] P. Saravanan, R. Gopalan, and V. Chandrasekaran, "Synthesis and Characterisation of Nanomaterials," 2008.
- [9] V. Srivastava, D. Gusain, and Y. C. Sharma, "Synthesis, characterization and application of zinc oxide nanoparticles (n-ZnO)," *Ceram Int.*, vol. 39, no. 8, pp. 9803–9808, Dec. 2013, doi: 10.1016/j.ceramint.2013.04.110.
- [10] V. M. Muinde, J. M. Onyari, B. Wamalwa, and J. N. Wabomba, "Adsorption of malachite green dye from aqueous solutions using mesoporous chitosan-zinc oxide composite material," *Environmental Chemistry and Ecotoxicology*, vol. 2, pp. 115–125, Jan. 2020, doi: 10.1016/j.enceco.2020.07.005.
- [11] T. M. Tamer et al., "Formation of zinc oxide nanoparticles using alginate as a template for purification of wastewater," *Environ Nanotechnol Monit Manag.*, vol. 10, pp. 112–121, Dec. 2018, doi: 10.1016/j.enmm.2018.04.006.
- [12] Z. Monsef Khoshhesab and S. Souhani, "Adsorptive removal of reactive dyes from aqueous solutions using zinc oxide nanoparticles," *Journal of the Chinese Chemical Society*, vol. 65, no. 12, pp. 1482–1490, Dec. 2018, doi: 10.1002/jccs.201700477.
- [13] R. Saravanan, V. K. Gupta, T. Prakash, V. Narayanan, and A. Stephen, "Synthesis, characterization and photocatalytic activity of novel Hg doped ZnO nanorods prepared by thermal decomposition method," *J Mol Liq.*, vol. 178, pp. 88–93, Feb. 2013, doi: 10.1016/j.molliq.2012.11.012.
- [14] R. Saravanan et al., "ZnO/Ag nanocomposite: An efficient catalyst for degradation studies of textile effluents under visible light," *Materials Science and Engineering C*, vol. 33, no. 4, pp. 2235–2244, May 2013, doi: 10.1016/j.msec.2013.01.046.
- [15] R. Saravanan et al., "ZnO/Ag/CdO nanocomposite for visible light-induced photocatalytic degradation of industrial textile effluents," *J Colloid Interface Sci.*, vol. 452, pp. 126–133, Aug. 2015, doi: 10.1016/j.jcis.2015.04.035.
- [16] R. Saravanan, V. K. Gupta, V. Narayanan, and A. Stephen, "Comparative study on photocatalytic activity of ZnO prepared by different methods," *J Mol Liq.*, vol. 181, pp. 133–141, May 2013, doi: 10.1016/j.molliq.2013.02.023
- [17] M. Ghaedi, F. N. Azad, K. Dashtian, S. Hajati, A. Goudarzi, and M. Soyak, "Central composite design and genetic algorithm applied for the optimization of ultrasonic-assisted removal of malachite green by ZnO Nanorod-loaded activated carbon," *Spectrochim Acta A Mol Biomol Spectrosc.*, vol. 167, pp. 157–164, Oct. 2016, doi: 10.1016/j.saa.2016.05.025.

- [18] J. N. Hasnidawani, H. N. Azlina, H. Norita, N. N. Bonnia, S. Ratim, and E. S. Ali, "Synthesis of ZnO Nanostructures Using Sol-Gel Method," *Procedia Chem.*, vol. 19, pp. 211–216, 2016, doi: 10.1016/j.proche.2016.03.095.
- [19] Madhusudan P, Yu J, Wang W, Cheng B, Liu G (2012) Facile synthesis of novel hierarchical graphene–Bi<sub>2</sub>O<sub>2</sub>CO<sub>3</sub> composites with enhanced photocatalytic performance under visible light. *Dalton Trans* 41(47):14345–14353.
- [20] Meng X, Zhang Z (2017) Bi<sub>2</sub>MoO<sub>6</sub> co-modified by reduced graphene oxide and palladium (Pd<sup>2+</sup> and Pd<sup>0</sup>) with enhanced photocatalytic decomposition of phenol. *Appl Catal B* 209:383–393.
- [21] Miao Y, Pan G, Huo Y, Li H (2013) Aerosol-spraying preparation of Bi<sub>2</sub>MoO<sub>6</sub>: a visible photocatalyst in hollow microspheres with a porous outer shell and enhanced activity. *Dyes Pigm* 99(2):382–389.
- [22] Nakata K, Fujishima A (2012) TiO<sub>2</sub> photocatalysis: design and applications. *J Photochem Photobiol, C* 13(3):169–189
- [23] Iriarte-Velasco U, Chimeno-Alanis N, Gonzalez-Marcos M P, et al. Relationship between Thermodynamic Data and Adsorption/Desorption Performance of Acid and Basic Dyes onto Activated Carbons[J]. *Chemical & Engineering Data*, 201 American Journal of Sciences and Engineering Research [www.ijournals.com](http://www.ijournals.com) 20 [www.ijournals.com](http://www.ijournals.com)
- [24] Acar E T, Ortaboy S, Atun G, et al. Adsorptive removal of thiazine dyes from aqueous solutions by oil shale and its oil processing residues: Characterization, equilibrium, kinetics and modeling studies[J]. *Chemical Engineering Journal*, 2015, 276: 340-348.
- [25] Bai S, Shen X, Zhong X, et al. One-pot solvothermal preparation of magnetic reduced graphene oxide-ferrite hybrids for organic dye removal[J]. *Carbon*, 2012, 50: 2337-2346.
- [26] Chen M, Huang Y, Chu W. et al. Exploring a broadened operating pH range for norfloxacin removal via simulated solar-light-mediated Bi<sub>2</sub>WO<sub>6</sub> process[J]. *Chinese Journal of Catalysis*, 2019, 40: 673-680.
- [27] Yu C, He H, Liu X, et al. Novel SiO<sub>2</sub> nanoparticle-decorated BiOCl nanosheets exhibiting high photocatalytic performances for the removal of organic pollutants[J]. *Chinese Journal of Catalysis*, 2019, 40: 1212-1221.
- [28] Yang K, Li X, Zeng D, et al. Review on heterophase/homophase junctions for efficient photocatalysis: The case of phase transition construction[J]. *Chinese Journal of Catalysis*, 2019, 40: 796-818.
- [29] Yu C, He H, Zhou W, et al. Novel rugby-ball-like Zn-3(PO<sub>4</sub>)<sub>2</sub>@C<sub>3</sub>N<sub>4</sub> photocatalyst with highly enhanced visible-light photocatalytic performance[J]. *Separation and Purification Technology*, 2019, 217: 137-146.
- [30] Hu J, Chen D, He J, et al. Recyclable Carbon Nanofibers@Hierarchical I-Doped Bi<sub>2</sub>O<sub>2</sub>CO<sub>3</sub>-MoS<sub>2</sub> Membranes for Highly Efficient Water Remediation under Visible-Light Irradiation [J]. *ACS Sustainable Chemistry & Engineering*, 2018, 6: 2676-2683.
- [31] Rahmani M, Sasani M. Evaluation of 3A zeolite as an adsorbent for the decolorization of rhodamine B dye in contaminated waters[J]. *Applied Chemistry*, 2016, 41: 83-90.
- [32] Hegazi H. Removal of heavy metals from wastewater using agricultural and industrial wastes as adsorbents[J]. *HBRC*, 2013, 93: 276-282.
- [33] Javaid A, Bajwa R, Shafique U, et al. Removal of heavy metals by adsorption on *Pleurotus ostreatus*[J]. *Biomass & Bioenergy*, 2011, 35: 1675-1682.
- [34] Mondal S. Methods of dye removal from dye house effluent-An overview[J]. *Environmental Engineering Science*, 2008, 25: 383-396.
- [35] Salleh M A M, Mahmoud D K, Karim W A W A, et al. Cationic and anionic dye adsorption by agricultural solid wastes: A comprehensive review[J]. *Desalination*, 2011, 280: 1-13.
- [36] Alizadeh R, Kazemi R K, Rezaei M R, et al. Ultrafast removal of heavy metals by tin oxide nanowires as new adsorbents in solid-phase extraction technique[J]. *International Journal of Environmental Science and Technology*, 2018, 15: 1641-1648.
- [37] Hu H, Srinivasan P. Mesoporous high-surface-area activated carbon[J]. *Microporous and Mesoporous Materials*, 2001, 43: 267-275
- [38] Selvam P, Preethi S, Basakaralingam P, et al. Removal of rhodamine B from aqueous solution by adsorption onto sodium montmorillonite[J]. *Hazardous Materials*, 2008, 155: 39-44.
- [39] R. Sivaraj, Pattanathu K.S.M. Rahman, P. Rajiv, Hasna Abdul Salam, R. Venkatesh Biogenic copper oxide nanoparticles synthesis using *Tabernaemontana divaricate* leaf extract and its antibacterial activity against urinary tract pathogen, *Spectrochim. Acta A Mol. Biomol. Spectrosc.*, 133 (2014), pp. 178-181
- [40] N.Z. Shah, N. Muhammad, S. Azeem, A. Rauf, Studies on the chemical constituents and antioxidant profile of *Conyza Canadensis*, *Midd-East J. Med. Plants Res.*, 1 (2012), pp. 32-35



10.22214/IJRASET



45.98



IMPACT FACTOR:  
7.129



IMPACT FACTOR:  
7.429



# INTERNATIONAL JOURNAL FOR RESEARCH

IN APPLIED SCIENCE & ENGINEERING TECHNOLOGY

Call : 08813907089  (24\*7 Support on Whatsapp)